Table 5.5 contd...

1	2	3	4†	5†	6	7	8†	9†
1551-205	19.12.80	0.450			31.10.81	0.391	y	y
	07.11.81	0.276	y	y	14.11.81	0.156		y
	13.11.82	0.178						
1601-209	19.12.80	0.414			06.11.81	0.331	y	y
	14.11.81	0.196		y	15.12.81	0.344		
	20.10.82	0.596	y		06.11.82	0.336	y	y
	13.11.82	0.218		y				
1615-201	19.12.80	0.362			14.12.81	0.274	y	y
	13.11.82	0.273	y	y				
1623-194	20.12.80	0.352			24.12.80	0.418	y	y
	06.11.81	0.412			09.12.81	0.162		y
	14.12.81	0.247						
1628-211	23.12.80	0.376	y	y	24.12.80	0.392		y
	14.11.81	0.305	y	y	18.12.81	0.288	y	y
	03.11.82	0.486						
1631-201	20.12.80	0.319			23.12.80	0.369	y	
	09.12.81	0.127		y	11.12.81	0.161		
	05.11.82	0.463	y	y				
1632-199	18.12.80	0.282	y	y	20.12.80	0.315	y	y
	23.12.80	0.365	y	y	10.11.81	0.384	y	y
	09.12.81	0.124		y	12.12.81	0.175		y
1637-196	18.12.80	0.265	y	y	23.12.80	0.348	y	y
	09.12.81	0.109		y	11.12.81	0.142		y
	03.11.82	0.514	y	y				
1655-201	24.12.80	0.298	y	y	12.12.81	0.092		y
	14.12.81	0.124						
1657-203	13.12.81	0.098			20.12.82	0.211	y	y
1700-204	25.12.80	0.293	y		14.12.81	0.103		
	16.12.81	0.136			18.12.81	0.170		y
	20.12.82	0.200		y				
1905-190	25.12.81	0.229	y	y	28.12.81	0.180		
	14.01.82	0.146		y				
1918-185	28.12.81	0.231	y	y	04.01.82	0.118		y
	15.01.82	0.115			05.01.83	0.107		
1933-173	30.01.79	0.298			07.01.82	0.134		
	05.01.83	0.169			Nonscintillating			
1938-167	07.01.82	0.157		y	09.01.82	0.129		
	05.01.83	0.192	y	y				
1945-168	08.01.82	0.164			10.01.82	0.133		
	08.01.83	0.168			Nonscintillating			
2014-157	06.01.82	0.305	y	y	09.01.82	0.256	y	y
	13.01.82	0.190		y	16.01.82	0.142		y

Table 5.5 contd....

1	2	3	4†	5†	6	7	8†	9†
2023-142	04.01.82	0.381	y	y	07.01.82	0.333	y	y
	10.01.82	0.284	y	y	13.01.82	0.236	y	y
	17.01.82	0.173		y	05.02.82	0.204		y
2105-119	14.01.82	0.386	y	y	17.01.82	0.337	y	y
	29.01.82	0.145		y	31.01.82	0.117		y
	25.02.82	0.355	y	y				
2120-102	22.02.79	0.243	y	y	24.02.79	0.275	y	y
	01.02.81	0.158		y	02.02.81	0.144		y
	03.02.81	0.131		y	19.01.82	0.369	y	y
	28.01.82	0.224	y	y				
2127-096	02.02.81	0.171			03.02.81	0.157		y
	04.02.81	0.142			20.02.82	0.187		y
	23.01.83	0.338	y	y				
2207-069	02.02.81	0.329	y	y	03.02.81	0.313	y	y
	04.02.81	0.296	y	y	05.02.81	0.280		
	06.02.81	0.264			07.02.81	0.247	y	y
	08.02.81	0.231	y	y	13.02.82	0.156		y
	14.02.82	0.141		y				
2211-057	04.02.81	0.322	y		25.02.82	0.100		y
	27.02.82	0.121		y				
2223-053	05.02.81	0.349			06.02.81	0.333		
	07.02.81	0.317	y	y	08.02.81	0.300	y	y
	02.03.82	0.115		y	17.03.82	0.349	y	y
	19.03.82	0.381		y				
2304-012	19.02.82	0.304	y	y	26.02.82	0.191		y
	28.02.82	0.160		y	13.03.82	0.115		y
	26.03.82	0.315	y	y				
2322+006	17.02.82	0.414	y	y	24.02.82	0.301		
	28.02.82	0.237	y	y	03.03.82	0.189		
	04.04.82	0.378						
2342+023	10.03.82	0.157		y	04.04.82	0.294		y
	10.04.82	0.389	y	y				
2356+033	13.04.81	0.380			10.03.82	0.213		
	13.03.82	0.164			Nonscintillating			

† 'y' in columns μ? and ψ? indicates that the observation was used to derive the values of μ and ψ respectively. A blank indicates that it was not used.

surveys of sources selected at metre wavelengths did not go below few Jansky (Harris & Hardebeck 1969, Readhead & Hewish 1974, Bhandari, Ananthakrishnan & Pramesh Rao 1974). Recently, Artyukh & Speed (1979) have complemented the earlier surveys by observing 64 sources at 102.5 MHz down to 0.5 Jy at 408 MHz. We have made IPS observations of 90 sources stronger than 0.75 Jy at 91.8 cm (326.5 MHz) and outside the Galactic plane ($|b^{II}| \geq 10°$) selected from the ninth Ooty lunar occultation list (Joshi & Singal 1980), which gives 91.8 cm radio structures and optical identifications above the PSS limit for an unbiased sample of 240 radio sources (on the Moon's path in the sky) and lists sources as weak as 0.25 Jy. Three sources (0311+175.1, .2, 0946+076) were not observed out of the 93 satisfying the above selection criteria because two of them (the first two) are too close to each other and hence confused in the telescope beam and one (the third) is confused with a nearby strong source (0945+076 ≡ 3C227≡4C07.29, 15.5 Jy at 408 MHz - Large et al. 1981) in the sky. The observation and reduction procedure has been described in sections 5.2 and 5.3 above.

5.4.1 The Statistics of ψ and μ Log of the observations and values of μ and ψ along with some supplementary information are listed in Tables 5.5 and 5.6 for the 90 sources. Since the range of flux densities for the sample is about 5 to 1 and that of angular sizes (LAS) about 100 to 1 (with over

Table 5.6   Data for the 90 Ooty occultation sources

Source	Op.Id.[†] code	91.8 cm occultation data			91.8 cm IPS data		α^{92}_{11}
		Flux/Jy	LAS/asec	Str.[#]	$\mu^{\star}$	$\psi/\text{asec}^{\star}$	
1	2	3	4	5	6	7	8
0045+076	G	0.90	15.7	S	<0.06	>1.	0.76
0054+078.2	EF	0.75	<3.7	U	0.424(4)	0.20(6)[§]	1.15
0054+090	EF	2.40	16.0	D	0.245(3)	0.20(5)	1.11
0146+133	G	0.75	29.5	S	0.289(1)	0.30(3)	0.89
0153+136	EF	2.00	25.0	D	0.300(3)	0.20(3)	0.88
0156+126	EF	1.00	42.0	D	0.190(3)	0.20(5)	0.83
0156+136	EF	1.20	<1.3	U	0.274(4)	0.20(5)	1.23
0200+130	EF	1.60	45.0	D	0.257(3)	0.30(4)	0.89
0202+149[0]	EF	4.30	<0.8	U	1.000	<0.02	0.18
0206+136	G	1.00	25.0	S	0.455(1)	0.4 (1)	0.55
0215+151	EF	1.00	<5.9	U	0.321(2)	0.70(3)	0.85
0232+150	EF	1.15	8.5	S	0.133(2)	0.65(2)	1.15
0237+154	EF	2.40	6.0	D	0.234(2)	0.30(3)	0.91
0309+175	G	0.90	<2.5	U	0.464(2)	0.15(3)	1.23
0312+180	EF	1.40	<3.3	U	<0.04	>1.	0.98
0325+180	EF	1.20	<10.0	U	0.296(2)	0.15(4)	0.83
0342+199	EF	0.80	4.7	PD	0.513(4)	0.15(4)	0.97
0343+184	EF	0.80	122.	D	0.049	>1.	1.02
0359+193	Q	1.40	<7.0	HT?	0.200(3)	0.10(3)[§]	0.53
0429+201	EF	1.35	8.8	D	0.186(4)	0.15(5)	0.85
0436+203	EF	1.60	43.0	S	0.150(1)	0.3 (1)	0.92
0453+205	EF	1.80	16.0	S	0.214(1)	0.25(3)	0.92
0512+209	EF	0.85	27.5	S	0.202(1)	0.3 (1)	0.98
0513+198	EF	0.80	28.0	D	0.305(1)	0.30(3)[1]	0.98
0708+184	G	2.20	16.0	D	<0.02	>1.	0.68
0736+167	EF	1.80	4.0	D	0.656(4)	0.25(4)[§]	1.10
0746+162	EF	1.40	3.4	PD	0.785(3)	0.10(5)	0.87
0748+164	Q	1.90	<2.0	U	0.510(2)	0.20(6)[2]	0.80
0806+152	G	1.50	26.5	D	0.220(3)	0.25(4)[§]	0.95
0852+124	EF	0.90	12.7	D	0.218(2)	0.05(3)	1.11
0853+121	EF	0.75	<4.7	U	0.449(4)	0.25(4)	1.05
0912+105	EF	0.85	10.5	S	0.226(3)	0.15(3)	0.68
0914+103	INP	0.80	15.0	S	<0.06	>1.	0.85
0915+099	EF	0.90	<6.5	U	0.622(3)	0.05(5)	0.33
0925+092	EF	1.50	12.5	D	0.315(4)	0.35(6)	1.01
0932+089	G	2.80	5.9	PD	0.187(3)	0.8 (1)	0.78
1007+062	EF	1.45	30.0	D	0.424(2)	0.25(3)	0.62
1033+038	EF	0.85	15.5	PD	0.052(1)	>1.	0.96
1039+035	EF	1.10	<4.2	HT?	<0.05	>1.	0.81

contd...

Table 5.6 contd...

1	2 †	3	4	5 #	6 *	7 *	8
1150-036	EF	0.95	34.0	D	0.237(4)	0.35(4)	0.98
1201-041	G	4.50	21.0	Cpx	0.097(3)	0.45(4)	0.59
1220-059	G	1.60	150.	D,Br	0.078(3)	0.35(3)	0.87
1232-064	EF	0.75	<2.5	U	0.595(3)	0.25(5)	0.77
1244-079	G	1.10	13.0	S	0.071(2)	0.20(2)	1.10
1246-081	EF	1.00	35.0	D	0.360(2)	0.40(2)	1.36
1249-086	INP	1.10	90.0	S	<0.05	0.2 (1)	1.02
1256-092	G	0.80	45.0	D	<0.06	0.6 (1)	0.55
1322-116	EF	2.00	7.6	D	0.301(4)	0.30(6)	1.04
1339-121.1	EF	2.00	<1.3	U	0.726(6)	<0.02(7)	0.72
1343-124	EF	1.00	10.0	PD	0.447(2)	0.30(5)	0.81
1344-127	EF	1.10	<2.2	U	0.533(7)	0.20(8)	0.86
1348-129	EF	3.50	1.2	S	0.918(15)	0.10(16)	0.90
1416-156	G	3.20	25.0	Cpx	0.190(4)	0.30(5)	0.53
1422-150	EF	1.60	150.0	D	0.217(1)	0.8 (1)	0.82
1426-161	G	1.60	21.5	S	<0.03	>1.	0.83
1429-154	EF	0.85	27.0	D	0.665(1)	0.3 (1)	1.01
1434-155	G	1.00	66.0	D	0.270(2)	0.05(2)	1.12
1445-161	G	2.80	<0.5	U	0.551(3)	0.05(6)	0.56
1452-168	Q	0.80	<11.0	U	0.315(2)	0.20(6)	0.67
1456-165	Q	1.50	3.0	S	0.485(7)	0.10(10)	0.99
1522-188	G	2.70	<1.8	U	0.729(4)	0.15(6)	0.81
1548-199	EF	1.10	20.0	D	0.149(2)	0.05(2)	0.75
1551-205	EF	0.80	3.2	S	0.428(2)	0.30(3)	0.73
1601-209	EF	0.75	<3.0	U	0.605(3)	0.40(4)	0.90
1615-201	EF	1.05	53.0	D	0.198(2)	0.40(2)	0.84
1623-194	EF	1.10	14.0	D	0.678(1)	0.70(2)	1.09
1628-211	EF	1.20	<1.7	U	0.437(3)	0.40(4)	0.92
1631-201	G	1.05	14.5	D	0.882(2)	0.85(2)	0.71
1632-199	EF	1.00	3.5	S	0.950(4)	0.15(6)	1.00
1637-196	EF	1.00	<1.7	U	0.527(3)	0.25(5)	0.92
1655-201	G	2.20	4.3	Cpx	0.135(1)	0.50(2)	0.90
1657-203	INP	0.80	43.0	D	0.455(1)	0.3 (1)	0.66
1700-204	EF	1.80	5.1	D	0.207(1)	0.35(2)	0.63
1905-190	Cwd	0.80	70.0	S	0.423(1)	0.60(2)	0.84
1918-185	EF	1.40	11.0	Cpx	0.422(1)	0.80(2)	1.01
1933-173	INP	2.00	188.0	D,Br	<0.03	>1.	0.87
1938-167	INP	0.85	37.0	PD	0.233(1)	0.20(2)	0.93
1945-168	EF	0.80	24.0	S	<0.06	>1.	0.77
2014-157	EF	0.85	<4.0	U	0.564(2)	0.25(4)	0.91
2023-142	G	1.00	2.7	S	0.354(4)	0.30(6)	1.20
2105-119	EF	1.20	<2.0	U	0.627(3)	0.20(5)	1.26
2120-102	EF	3.10	<0.8	U	0.589(4)	0.10(7)	0.91
2127-096	G	1.30	16.5	PD	0.243(1)	0.35(3)	0.79

Table 5.6 contd...

1	2[†]	3	4	5[#]	6[*]	7[*]	8
2207-069	EF	1.35	<2.3	U	0.502(5)	0.15(7)[§]	0.84
2211-057	EF	0.80	11.0	S	0.276(1)	0.35(2)	0.87
2223-053	G	1.40	<2.0	U	0.927(3)	0.15(5)[3]	0.78
2304-012	EF	1.15	<1.9	U	0.799(2)	0.40(5)	0.86
2322+006	EF	0.75	<7.0	U	0.659(2)	0.40(2)	1.09
2342+023	G	0.80	30.0	D	0.424(1)	0.10(3)[§]	0.75
2356+033	EF	1.25	17.0	S	<0.04	>1.	0.92

[†] G = galaxy or red object, EF = empty field to PSS limit, Q = quasi-stellar, red/blue stellar or blue object, INP = identification not possible, Cwd = crowded field

[#] Structure code: U = unidentified, S = single, D = double, PD = probable double, HT = head-tail, Cpx = complex, Br = bridge

[*] Number in parentheses is the number of observations used to derive the value.

[§] Scintillating structure is complex.

[0] 0202+149 has been extensively observed by Pramesh Rao (1975) in 1971.

[1] Two components of sizes 0.15 and 0.65 arcsec.

[2] Two components of sizes 0.10 and 0.30 arcsec.

[3] Confusing source: 2223-052 ≡ 3C 446.
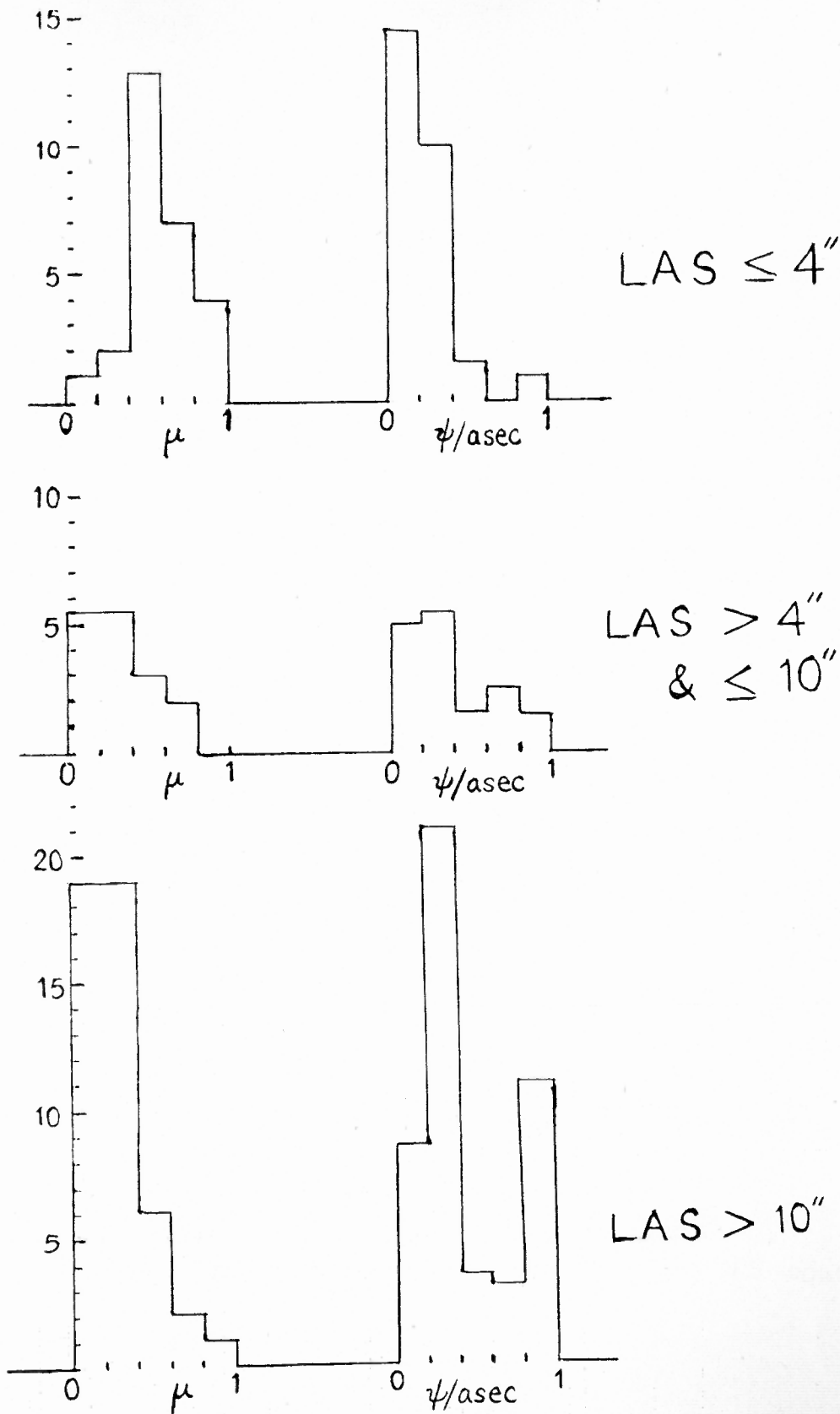
Fig.5.4 Observed distributions of the compactness parameter μ and the (mean) angular size of the compact structure ψ for the 90 Ooty occultation sources for 3 ranges of LAS.

Fig. 5.5 ψ vs μ scatter diagram for the 90 Ooty IPS sources

(5-35 ...)

half of the sources between 4 and 40 arcsec), we have looked

for any possible correlations among the source properties.

For this purpose, we have divided the sample into three ranges

of LAS: ≤ 4 arcsec, 4 to 10 arcsec and > 10 arcsec. Fig. 5.4

presents histograms of ψ and μ for the three classes. The

scatter diagram of ψ vs μ (Fig. 5.5) also brings out the trend

seen in this figure - we see that the top right-hand quadrant

is empty, that is, strong scintillators are more compact. This

and other trends are also brought out in Table 5.7, where we

have listed median values of various parameters for the three

Table 5.7   Properties of the 3 LAS classes of the 90 Ooty occultation
radio sources

LAS class	No. of srcs	μ_{med}	S_{92med} (Jy)	$\psi^{\#}_{med}$ (arcsec)	LAS_{med} (arcsec)	$\alpha^{92 \S}_{11med}$
LAS$\leq$4"	27	0.57	1.28	0.19	2.2	1.0
4"<LAS$\leq$10"	16	0.26	1.23	0.32	6.3	0.88
10"<LAS	47	0.23	1.05	0.33	25.	0.92
All	90	0.30	1.12	0.28	11.2	0.9

\#   The values are $10^{**}(\log \psi)_{med}$.

\S   These are only rough values

LAS classes. The spectral index α^{92}_{11} between 11.1 cm (2700 MHz)

and 91.8 cm was kindly provided by Gopal-Krishna from his flux

Fig.5.6 μ vs α scatter diagram for the 90 Ooty IPS sources
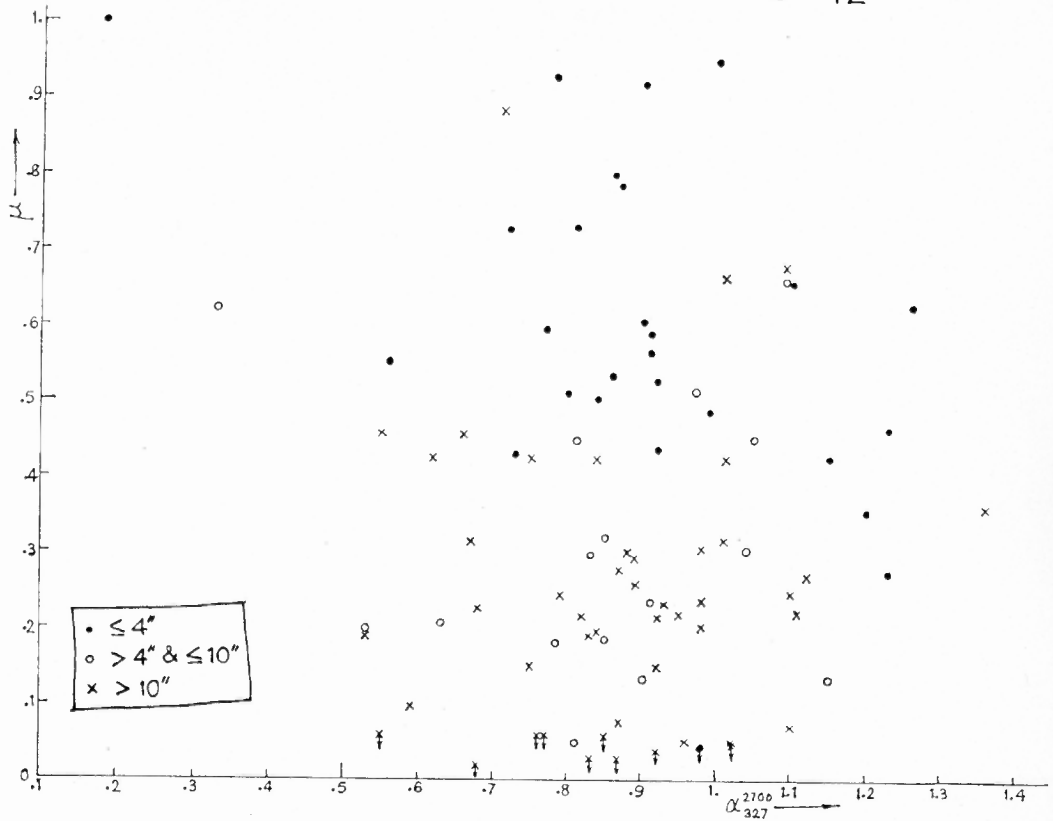
Fig. 5.7 ψ vs α scatter diagram for the 90 Ooty IPS sources
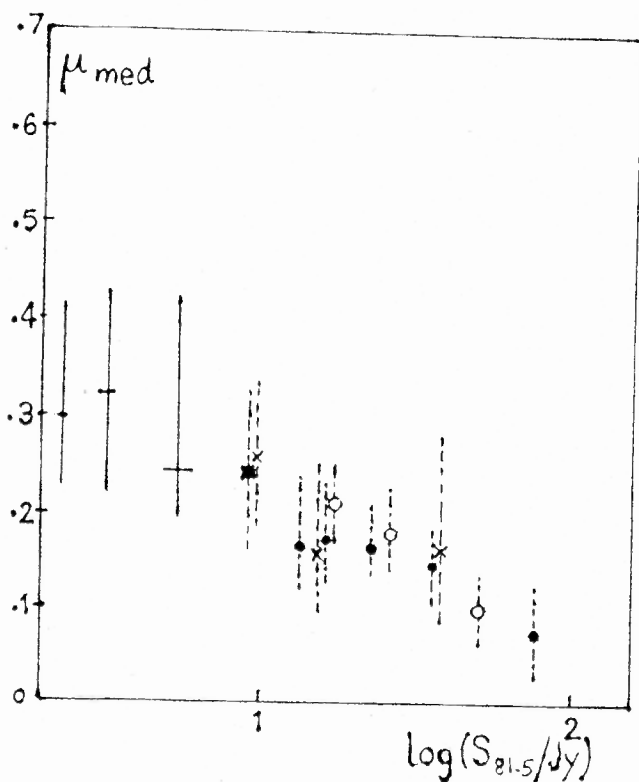
Fig.5.7a Three new points plotted on the revised μ-log$S_{81.5}$
diagram of Swarup & Bhandari (1976 ApLett 17 31). A spectral
index of 0.75 is used for converting 326.5 MHz flux densities
to 81.5 MHz. The 81.5 MHz μ-values have been revised by
a factor 0.6 as per Readhead et al. (1978). The other points
from Swarup & Bhandari's diagram have been revised
nominally assuming a scintillation index 0.6 for CTA21.

$(5-41...)$

density measurements with the 100m Effelsberg telescope. The

scatter diagram μ vs α_{11}^{92} (Fig. 5.6) shows no clear correla-

tion. The trend for ψ vs α_{11}^{92} (Fig. 5.7) is also not clear,

but among the smaller sources (≤ 10 arcsec - all but two of

these have $\alpha_{11}^{92} > 0.5$) those with more compact scintillating

components (small ψ) have less steep spectrum (α_{11}^{92} small)

whereas there is no clear correlation for the larger sources

(>10 arcsec).

We have divided the sample of 90 sources into three

ranges of flux densities 0.75 to 1.0, 1.0 to 1.4 and 1.4 to

4.5 Jy and calculated the median values of μ for the three

subsamples. After renormalizing the μ-S diagram of Swarup

& Bhandari (1976), these three new μ-S points fit very well

into the μ-S relation and confirm the saturation of this

relation toward low values of S reported by Speed & Warwick

(1978) and Artyukh & Speed (1979). (Fig. 5.7a gives a preliminary plot of
$\mu - \log S_{81.5}$, converting the 3 new points from 326.5 MHz to 81.5 MHz using a spectral index
of 0.75.)

5.4.2   The ψ_{IPS} - LAS Relation for Extragalactic Radio Sources

Fig. 5.8 shows the size of the scintillating structure $\psi_{326.5}$

plotted against the LAS for the three LAS ranges. The median

values are plotted, and the horizontal and vertical bars

extend from 33 to 67 percentile values, which is a simple and

completely nonparametric way of giving error bars on the median.

Sources which do not scintillate were taken to have a lower

limit of 1 arcsec to $\psi_{326.5}$.   There are 11 such sources out of
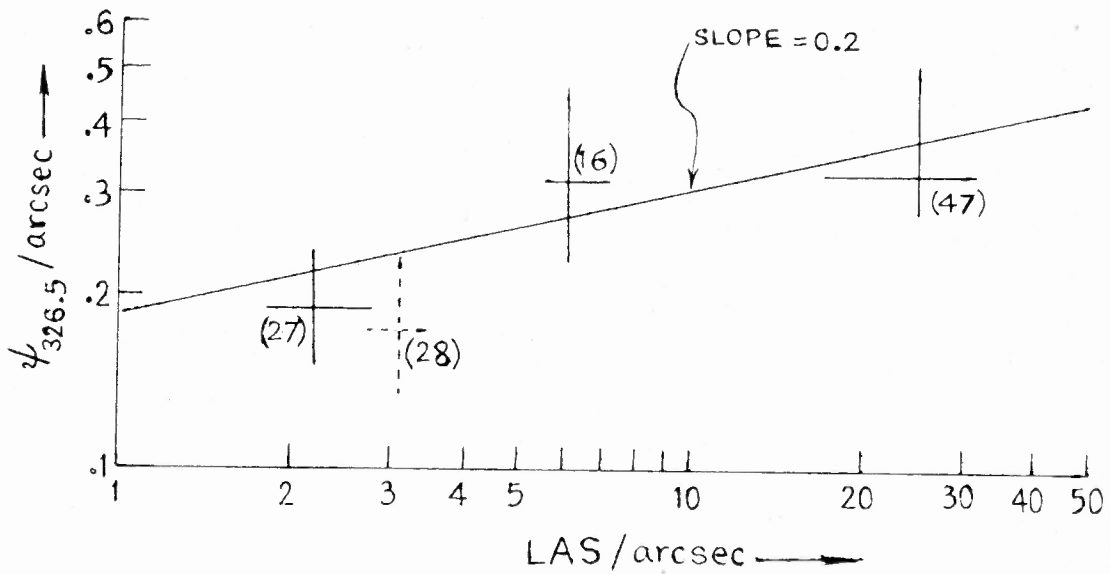
Fig. 5.8 $\psi_{326.5}$ - LAS relation (median values) on log-log scale. (The point with 28 sources is plotted for comparison. It is not used in the least-squares line.)
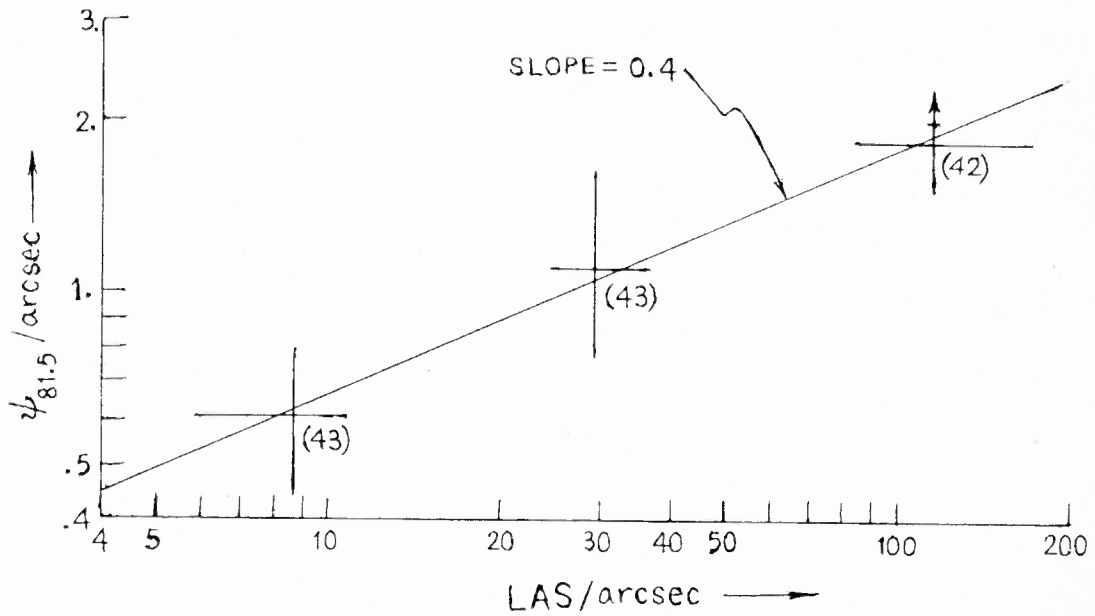
Fig. 5.9 The $\psi_{81.5}$–LAS relation (median values) on log-log scale

the total of 90 (i.e., 12%). The point corresponding to 326.5 MHz IPS observations of 28 steep-spectrum sources stronger than 1 Jy and of LAS between 1 and 4 arcsec (section 5.3) is also plotted. Fig. 5.9 shows a similar plot for 128 identified powerful edge-brightened (Fanaroff-Riley class II (1974)) doubles from the 3CR sample. Values of the size of the scintillating structure $\psi_{81.5}$ were taken from Readhead & Hewish's compilation (1974; 1976), modified according to Readhead et al. (1978), and corrected for interstellar scattering, where necessary, as per Duffett-Smith & Readhead (1976). The sources designated nonscintillating by Readhead & Hewish were taken to have a lower limit of 2 arcsec for $\psi_{81.5}$. There are 42 such sources out of the total of 128 (i.e., 33%). The three plotted points correspond to the three LAS ranges 1 to 16.5 arcsec, 16.5 to 57 arcsec and >57 arcsec, chosen to roughly equalize the number of sources in the three bins. It is clear that there is a correlation between log ψ and log LAS over a large range of LAS. The slope of the relation between the median values of log ψ and log LAS is significantly less than one, for the faint Ooty sample as well as the strong 3CR sample.

5.4.3 <u>Difference between the correlations for the Ooty and 3CR samples</u> However, there are also significant differences in the plots for the Ooty and 3CR samples. The slope of the median log $\psi_{326.5}$ vs log LAS relation is 0.2 (Fig.5.8), smaller than the slope 0.4 of the corresponding relation from

81.5 MHz IPS data (Fig. 5.9). It is also apparent that the mean scintillating size at 81.5 MHz is about 4 times that at 326.5 MHz. To explain the difference in <u>sizes</u>, first note that the scintillating sizes $\psi_{326.5}$ for the Ooty sources have been determined from the widths of the power spectra of scintillations at different elongations (as described in section 5.2), whereas values of $\psi_{81.5}$ were found from the scintillation indices at different elongations. This difference in the methods of deriving ψ as well as the fact that at lower frequencies, scintillation arises from intrinsically larger features lead to a higher value of $\psi_{81.5}$ compared to $\psi_{326.5}$ by a factor of about 2 (Ananthakrishnan 1976). The remaining factor of 2 is then easily seen to be due to the different mean LAS values for the two samples. (In addition, the intrinsic size to same optical depth at 81.5 MHz is expected to be larger than that at 326.5 MHz because of synchrotron self- absorption between these two frequencies. But this only marginally enhances $\psi_{81.5}$ over $\psi_{326.5}$ (Ananthakrishnan 1976).)

It is also perhaps relevant that the Ooty sample is an order of magnitude fainter and hence cosmologically more distant (Kapahi 1975; Swarup et al. 1982) than the 3CR sample. The effects of cosmological evolution are then expected to play a part. In this connection, it is worth mentioning that the Ooty sample is at the maximum in the differential
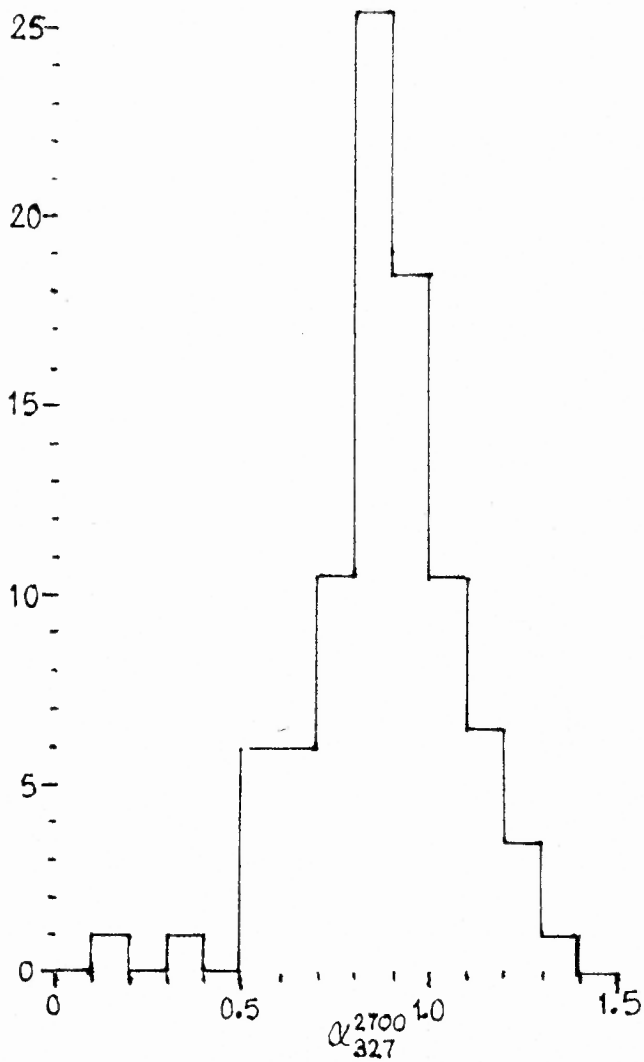
Fig. 5.10 Observed distribution of spectral indices α_{327}^{2700} for the unbiased sample of 90 faint Ooty sources

source count at metre-wavelengths (e.g., Wall 1980). However, since the whole factor of about 4 can be adequately accounted for as explained above, cosmological effects are probably unimportant in causing the grossly different scintillating sizes found for the two samples.

Coming to the different slopes for the two samples, we first show that the Ooty sources are likely to be steep-spectrum edge-brightened powerful doubles, similar to the 3CR sources. Though both samples are flux-limited, Ooty sample includes all sources above the limit, whereas only the edge-brightened FR II doubles above the 3CR flux limit have been selected for the 3CR sample. However, sources selected at metre-wavelengths generally have steep spectra, as is borne out by the distribution of spectral indices for the Ooty sample (Fig. 5.10). Only two out of the 90 sources have $\alpha^{2700}_{326.5} < 0.5$ and the median α is 0.9, which means contamination by flat-spectrum cores is negligible. It is not immediately possible to pick the edge-brightened Ooty sources from the lunar occultation profiles using the criterion of Fanaroff & Riley (1974) (or a similar structure-dependent one), nor are the optical identifications complete enough to separate the less powerful sources from the more powerful ones using estimates of the luminosity. However, there is indirect evidence from the angular size-flux density relation (Kapahi 1975) and the identification content of samples of faint radio sources

$(S_{327} \sim 1$ Jy) (Swarup, Subrahmanya & Venkatakrishna 1982) to suppose that the Ooty sources are from a distant powerful population. Since projection and blending of more than one compact feature to give a single ψ-value are expected to cause a similar flattening (see next section) for both the samples, apart from any difference in slopes in the log ψ - log LAS correlation due to contamination of the Ooty sample by less powerful sources, the slopes for the two samples seem to be genuinely different, and not due to the different frequencies and methods used in determining ψ.

The most likely candidates for the scintillating struc-ture are hotspots fed by jets (see next section). The dif-ferent slopes could then be partially due to the confining agent for the jets being the interstellar medium for the sources in Fig. 5.8 which have smaller LAS values, whereas for the larger sources of Fig. 5.9, it is the intergalactic medium. For an assumed size 15 kpc for the extent of the interstellar medium (ISM) from the centre of the parent object, the minimum angular size (with $H_O = 50$ km/s/Mpc and the Einstein-de Sitter world model) is about 2 arcsec. Secondly, the mean redshift of the smaller 3CR sources is much higher than that of the larger ones whereas the spread in redshifts of the much fainter and hence farther (Kapahi 1975; Swarup et al. 1982) Ooty sample is probably much less. Since the angular size is inversely related to redshift if the hotspot linear size is
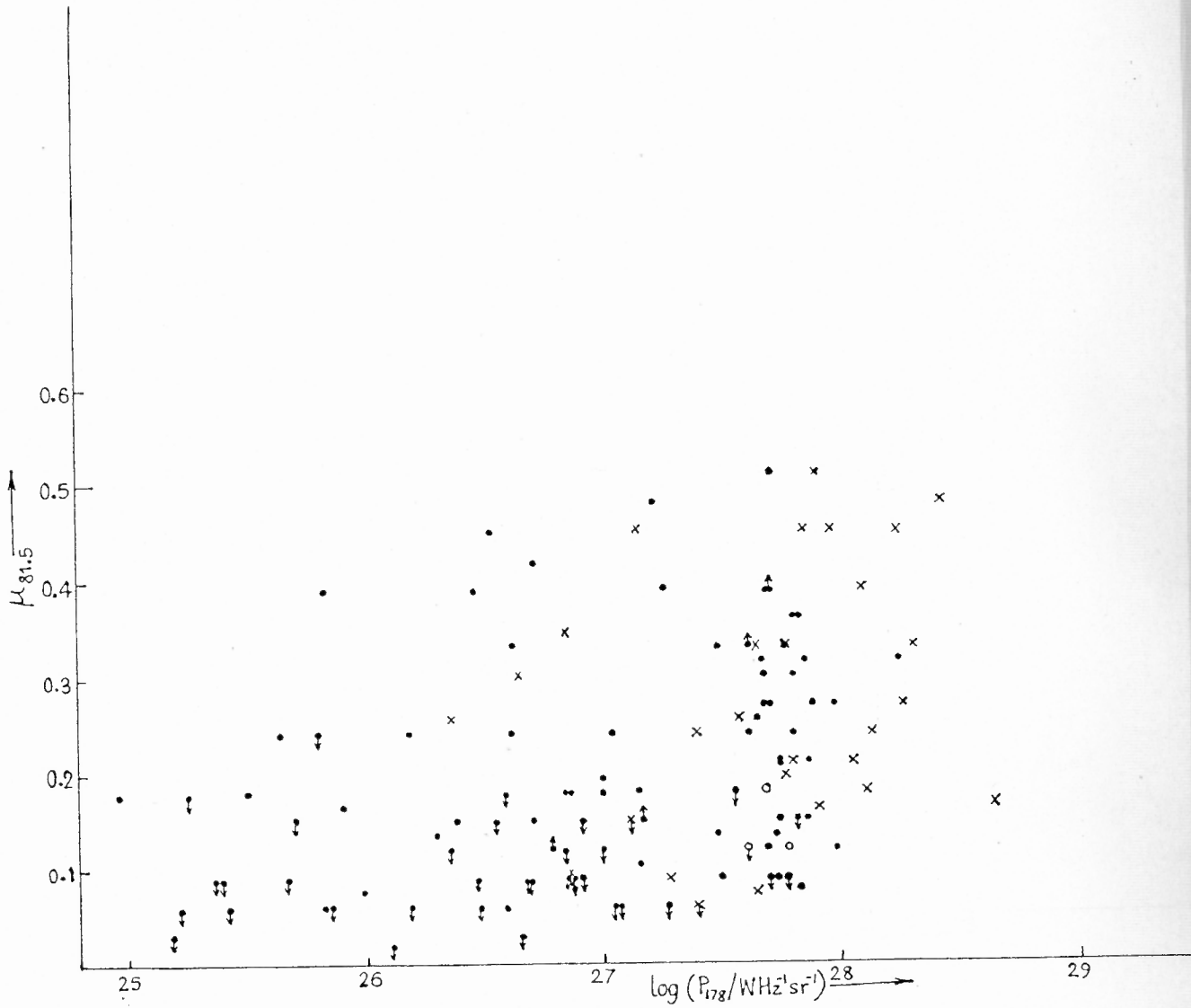
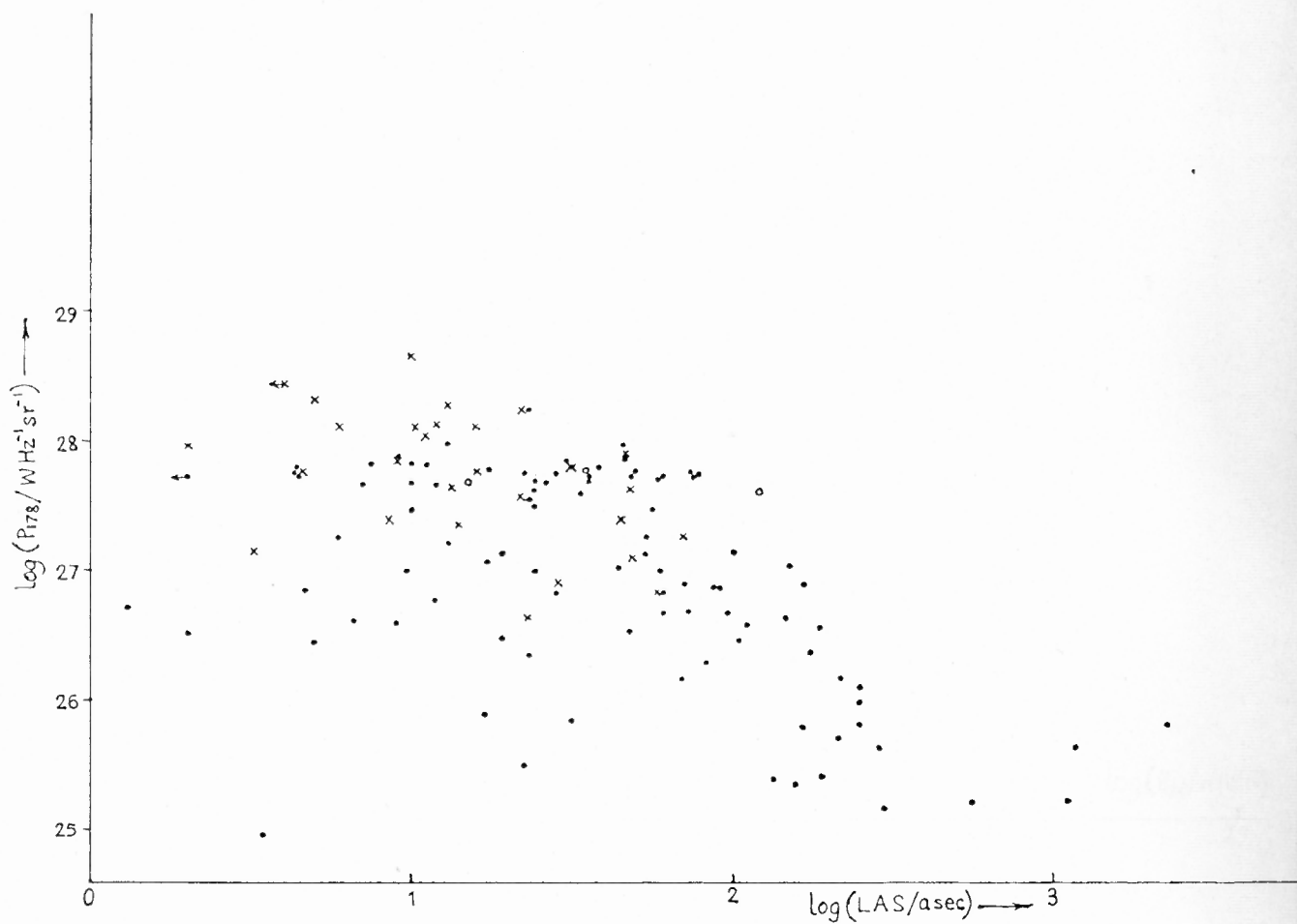Fig. 5.11 $\mu_{81.5}$ - log P_{178} scatter diagram for the optically identified FRII 3CR radio sources

Fig. 5.12 log P_{178} - log LAS scatter diagram for the optically identified FR II 3CR sources
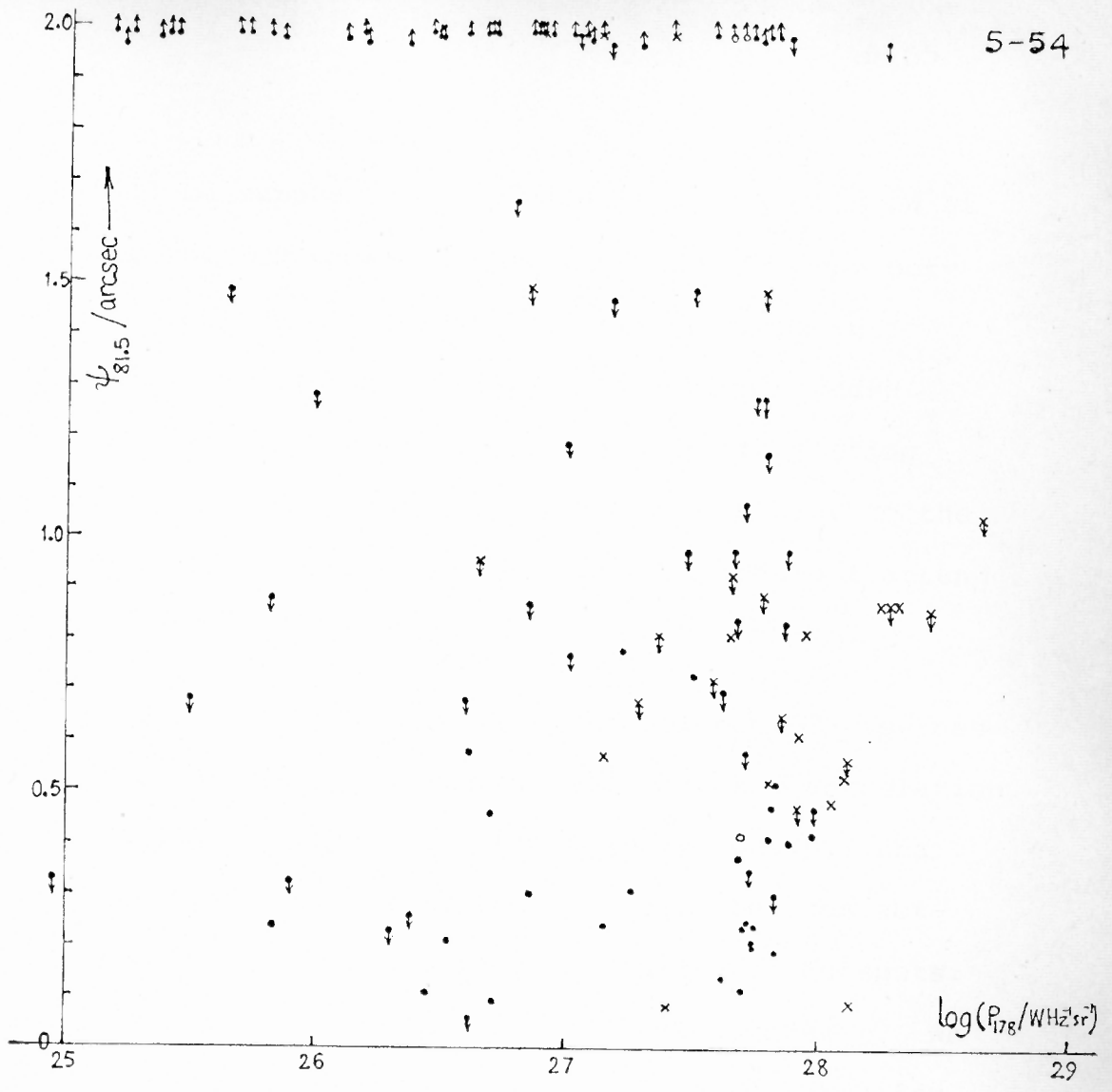
Fig. 5.13 $\psi_{81.5}$ – $\log P_{178}$ scatter diagram for the optically identified FRII 3CR radio sources

(5-51...)

constant, ψ will be suppressed at smaller LAS and enhanced at larger ones for the 3CR sources but not so much for the Ooty sources. This could be a cause of the steeper slope in Fig. 5.9 compared to that in Fig. 5.8. As a simpleminded calculation to test this, it can be shown that translating the ψ-values of the largest and the smallest LAS bins to the mean redshift of the intermediate LAS bin does indeed flatten the relation in Fig. 5.9 sufficiently.

The log $\psi_{81.5}$ - log LAS correlation for the 3CR sources cannot be explained from the luminosity-compactness correlation found for 3CR sources (Jenkins & McEllin 1977; Swarup, Sinha & Hilldrup 1984) from aperture synthesis maps. The compactness is measured by the fraction of flux density in hotspots. The analogous IPS parameter is the scintillation index μ. We do indeed find that μ and log P_{178} are mildly correlated for the 128 3CR sources (Fig.5.11). To see directly if the large range in luminosity gives rise to the log $\psi_{81.5}$ - log LAS correlation, we examined log P_{178} vs log LAS and $\psi_{81.5}$ vs log P_{178}. The first shows a good anticorrelation (Fig. 5.12), consistent with the LAS-z diagram and the tight correlation between z and luminosity for the 3CR sample (see, e.g., Kapahi 1978). To explain the log $\psi_{81.5}$ - log LAS correlation, an anticorrelation between $\psi_{81.5}$ and log P_{178} is required, but we find a scatter diagram instead (Fig. 5.13).

To summarize, the <u>slopes</u> of the log ψ - log LAS relations

for the faint Ooty and bright 3CR samples are different (Figs. 5.8 and 5.9) mainly because the redshift range for the 3CR sample is much larger than the probable range for the Ooty sample. There is a <u>break</u> in these relations corresponding to a factor of about 4 in ψ because the mean LAS of the two samples are different and also due to the different methods of determining ψ from the scintillation data for the two samples.

5.4.4 The ψ_{HS}-θ relation from VLA observations of hotspots in powerful double radio sources

The beams which feed the two outer components of extended double radio sources are visible as jets in sources of low power, which do not have bright hotspots at the ends of the radio lobes. In more powerful sources, the beams are not visible as jets in maps of the best currently available dynamic range and end in bright, compact hotspots. Whether these extragalactic beams expand freely or are collimated as they extend from the central core to the outer hotspots is an open question, though evidence seems to show that they do not expand freely throughout their length (Bridle 1982). A plot of the hotspot (angular) size ψ_{HS} versus (angular) distance from the core θ for the bright hotspots from 4.87 GHz VLA observations of a sample of the largest quasars at various redshifts (Swarup, Sinha & Hilldrup 1984) shows a tight relation. We present this result below and discuss its implications.

About the only method to get information on the subarcsec

Fig. 5.14 f_c – log l diagram for the 31 hotspots of Swarup et al. (1984)

structure of substantial samples of extended extragalactic
radio sources till recently was IPS, though some VLBI studies
of hotspots in radio sources have also been carried out
(Kapahi & Schilizzi 1979, Barthel 1983). The Very Large Array
(VLA) can now give such a resolution at centimetre wavelengths
so that it is possible to study the structure of various
parts of extended sources in detail, in particular, the hot-
spots. Swarup, Sinha & Hilldrup (1984) have mapped at 4.87 GHz
(6 cm) 31 quasars chosen from the 3CR, 4C and B2 samples as
having the largest angular sizes at various redshifts (i.e.,
those near the upper envelope of the LAS-z diagram) (see also
Swarup, Sinha & Salter 1982). These 31 sources do not show
any correlation between the fraction of flux density in the
central component and the projected linear size (Fig. 5.14).
This means that projection effects are minimal for the sample
(Kapahi & Saikia 1982). Swarup et al. (1982, 1984) have selec-
ted more 3CR sources at lower redshifts and more 4C and B2
sources at higher redshifts to minimize the radio luminosity
range. This minimizes the spread in other properties which
may be correlated with the radio luminosity. We have selected
the 14 bright and/or compact hotspots from these maps and
determined their size ψ_{HS} perpendicular to the source major
axis and the distance θ of the hotspots from the core. Keeping
in mind the possibility that only the lobe on one side may be
fed by the beam at a time (Rudnick 1982, Rudnick & Edgar 1984),
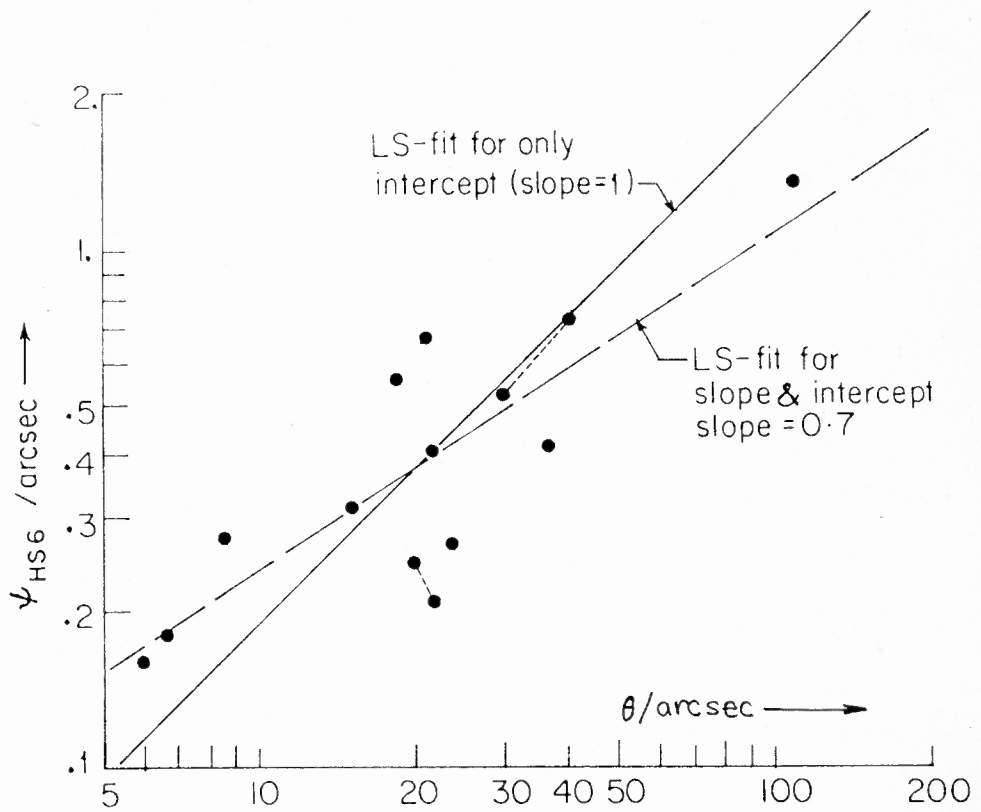we chose the more compact hotspot from a given source. For two

Fig. 5.15 ψ_{HS}- θ relation (on log-log scale) for the 14 brightest and/or most compact hotspots from Swarup et al. (1984)

sources, such a decision was difficult, so we took hotspots from both the sides. We have not included any diffuse or low brightness hotspots. The 14 hotspots are listed in Table 5.8 and ψ_{HS} vs θ is shown as a log-log plot in Fig. 5.15. The best linear fit has a slope close to 1.

Table 5.8   The hotspots used

0118+03 SE	0133+20 SW	0229+34 NW1	0312-03 NE,SW2
0835+58 SW1	0932+02 NE	0957+00 NW1	1248+30 SW
1545+21 SW2	1545+21 NE1	1622+23 SW2	1739+18 NW1
2325+29 SE2			

Before attempting a quantitative interpretation of the ψ_{HS}- θ relation, two points must be noted. The jet is necessarily confined till it has emerged from the relatively dense interstellar medium (ISM) into the rarer intergalactic medium. The minimum angular size corresponding to the ISM is about 2 arcsec (see section 5.4.3), well below the smallest value of θ in Fig. 5.15. Secondly, the ψ_{HS} - θ relation does not depend on the ages (or evolutionary stages) of the sources used, provided ψ_{HS} is a good representation of the beam extent in cross section. The reason for this is clear for a free beam (see equation 5.2 below). It is true even for a confined beam, because the confinement (and hence the value of ψ_{HS}) is governed

by the balance of the ambient pressure and the centripetal pressure bending the fluid trajectory within the walls of the beam, whereas θ is determined by a ram pressure balance at the hotspot. In both these pressure balances, the product of the density of the ambient medium with the beam velocity, $\rho.V$, and the momentum flux in the beam occur in identical ways, so that the final $\psi_{HS} - \theta$ relation is independent of all the three parameters (Eichler 1983). Since we have chosen only the most compact and/or intense hotspots, ψ_{HS} represents the beam extent in cross section.

A proportionality between ψ_{HS} and θ as implied by Fig. 5.15, however, does not necessarily entail a freely expanding beam. Eichler (1983) has shown that even a beam expanding in a homogeneous medium can be collimated several times before it impinges on the medium. Assuming that Eichler's maximum channel width determines ψ_{HS} and that the distance to the head of the beam is determined by ram pressure balance, we have derived a proportionality between ψ_{HS} and θ:

$$\psi_{HS} = [(2(1-\cos\phi_o)/\pi)^{\frac{1}{2}}.\delta\phi].\theta, \qquad \dots \qquad (5.1)$$

where ϕ_o is the semiangle of opening of the channel at the core and the intrinsic beam opening angle $\delta\phi$ is taken $<< \phi_o$. For a free beam, the proportionality constant between ψ_{HS} and θ is much larger, because $\delta\phi = 2\phi_o$, and

$$\psi_{HS} = [2\tan\phi_o].\theta. \qquad \dots \qquad (5.2)$$

The intrinsic beam opening angle $\delta\phi$ is different from the channel opening angle $2\phi_o$ because of jitter or fast precession (cf Scheuer's dentist's drill (1982)). Eichler's treatment only requires that the cause of making the channel broader than the actual beam be (roughly) axisymmetric (thereby defining the channel axis). Though the slope of the linear fit in Fig. 5.15 is 0.7, if we force the slope to unity, we get $\delta\phi \simeq 0.1$ deg for $\phi_o = 15$ to 20 deg from equation 5.1 . On the other hand, a free beam is required to be stable and as narrow as about 1 deg (equation 5.2).

To find out and understand the structure and dynamics of extragalactic beams, both high resolution observations and theoretical (including numerical) calculations are required. Whether the most powerful beams are invisible and the less powerful ones visible through dissipation at the walls, or all beams are in principle visible, given sufficient sensitivity and dynamic range, both kinds of sources: those with easily visible beams (i.e., those with (radio) jets) and those with other evidence (like hotspots) for beams need to be studied with finer resolution, sensitivity and higher dynamic range than are currently available, with especial stress on improving the dynamic range so that structures on all scales can be studied in conjunction. As an example of such a study, see Perley Dreher & Cowan (1984) who have detected an extended radio jet and several rings in the lobes in 1957+405 ($\equiv$ Cyg A $\equiv$ 3C405).

Having presented the relation between the hotspot size
and the distance to the core, we should add that the selection
of the hotspots is not based on any objective quantitative
criterion, but just inspection of the maps. To establish the
relation properly, it is necessary to investigate larger
samples of hotspots chosen, using an objective quantitative
criterion, to ensure that the transverse hotspot extent repre-
sents the width of the beam feeding them.

5.4.5 Connection between the $\psi_{HS} - \theta$ and $\psi_{IPS} -$ LAS relations

Extended extragalactic radio sources selected at low frequencies
have a steep radio spectrum. Only the central core has a
flat or inverted spectrum and emits as much as the outer com-
ponents only at centimetre-wavelengths. Almost all the
emission at metre-wavelengths is from the steep-spectrum outer
components. (See sections 1.2 and **5**.4.1.) Hence the scintilla-
ting structure in the IPS observations most likely represents
hotspots. The flat relation between (the median values of)
$\log \psi$ and $\log$ LAS (Figs. 5.8 and 5.9) then indicates, at face
value, that extragalactic jets do not expand freely. If
they did ψ would be proportional to LAS (on an average) and
the slope of the relation would be unity. But a roughly unit
slope is precisely what the $\log \psi_{HS} - \log \theta$ plot (Fig. 5.15
above - section 5.4.4) shows! The sources used are from the
upper envelope of the LAS-z diagram and hence have little pro-
jection effects. The hotspot size, taken as the jet extent in

cross section, should not suffer any shortening due to pro-
jection, but the distance from the core θ would reduce. This
reduction would increase the number of sources with smaller
apparent θ (and also LAS). Hence any projection effects in
the IPS samples will decrease the slope 0.7 of the relation
of section 5.4.4 and also increase its scatter. This slope
should thus be taken as the maximum slope such a relation
will show. There are two more reasons why the slopes in
Figs. 5.8 and 5.9 are smaller. Firstly, the IPS technique
gives a weighted mean of the sizes of all the bright compo-
nents in a source. This includes the brighter parts of the
lobes in addition to the hotspots. And this enhancement in
ψ is more for smaller LAS sources. Secondly, there is no
way IPS can distinguish between bright components on the two
sides if the whole source is within the telescope beam. This
again acts most strongly for the smallest LAS sources. These
two effects then tend to produce a higher ψ-value for lower
LAS values, thereby flattening the log ψ - log LAS relation,
which is further flattened due to projection effects.

To trace the effect of projection, we divided the
128 3CR sources into three redshift ranges: 0 to 0.2, 0.2 to
0.6 and 0.6 to 2.1. Restricting only to sources of the
largest LAS values in these three bins and plotting the
median values of log $\psi_{81.5}$ vs log LAS gave the slope of
0.51. For sources of the intermediate and smallest LAS values,

the slopes were 0.40 and 0.22. The overall slope 0.43
(Fig. 5.9) is intermediate among these. This shows that
projection does indeed flatten the log ψ - log LAS relation.
However, since the slope 0.51 for the largest sources is
significantly lower than 0.7, projection does not explain
all the flattening.